HHS Public Access

Author manuscript

Ultrasound Med Biol. Author manuscript; available in PMC 2021 June 01.

Published in final edited form as:

Ultrasound Med Biol. 2020 June ; 46(6): 1474–1489. doi:10.1016/j.ultrasmedbio.2020.01.029.

Imaging the activation of low-boiling-point phase-change contrast agents in the presence of tissue motion using ultrafast inter-frame activation ultrasound imaging

Bowen Jing[a], **Milton E. Brown**[a], **Michael E. Davis**[a,b,c], **Brooks D. Lindsey**[*,a,d]

[a]Wallace H Coulter Department of Biomedical Engineering, Georgia Institute of Technology and Emory University, Atlanta, GA, USA

[b]Children's Heart Research & Outcomes Center, Children's Healthcare of Atlanta & Emory University, Atlanta, GA 30322, USA

[c]Division of Cardiology, Department of Medicine, Emory University, Atlanta, GA 30322, USA

[d]School of Electrical and Computer Engineering, Georgia Institute of Technology, Atlanta, GA 30313, USA

Abstract

Nanoscale phase change contrast agents (PCCAs) have been demonstrated to represent great potential for non-invasive extravascular imaging and therapeutic delivery. However, the contrast-to-tissue ratio (CTR) of PCCA images is usually limited due to either physiological motion or incomplete cancelation of tissue signal. Therefore, to improve the CTR of PCCA images in the presence of physiological motion, a new imaging technique, ultrafast inter-frame activation ultrasound (UIAU) imaging, is proposed and validated. Results of studies with controlled motion in tissue-mimicking phantoms indicate UIAU could provide significantly higher CTR (maximum: 17.3±0.9 dB) relative to conventional pulse inversion imaging (maximum CTR: 3.4±1.4 dB). UIAU exhibits a CTR of up to 16.1±1.0 dB relative to 3.9±2.3 dB for differential imaging in the presence of physiological motion at 20 mm/s. In vivo imaging of PCCAs in the rat liver also demonstrate the ability of UIAU for enhancing PCCA image contrast in the presence of physiological motion.

Keywords

Contrast-to-tissue ratio; extravascular imaging; molecular imaging; nanoscale phase change contrast agents; ultrafast inter-frame activation ultrasound

[*]Author for correspondence: brooks.lindsey@bme.gatech.edu, 404-385-6647.

Introduction:

Many previous studies have reported the use of ultrasound and microbubbles to successfully deliver therapeutics such as siRNA, miRNA, or genes in animal models (Bez, et al. 2019, Hernot and Klibanov 2008). This approach is promising due to the ability for non-invasive, focused delivery with image guidance. While microbubbles are required to modulate delivery, these agents are limited to vascular spaces due to their relatively large size (~1–10 μm). Alternatively, the use of low-boiling point phase change contrast agents (PCCA) for diagnostic ultrasound imaging has been previously explored in a number of in vitro and preclinical studies. The volatile perfluorocarbon core in the PCCA can be vaporized (or "activated") from liquid to gas form after injection by applying external energy such as laser pulses (Hannah, et al. 2016, Lin, et al. 2017, Strohm, et al. 2011, Yoon, et al. 2017) and ultrasound pulses (Apfel 1998, Cao, et al. 2018, Ho and Yeh 2017, Kang, et al. 2014, Kripfgans, et al. 2000, Sheeran, et al. 2011), thus transforming hypoechoic nanoscale droplets into echogenic gaseous microbubbles that can be visualized in ultrasound images.

Compared with the conventional ultrasound contrast agent, microbubbles, there are several advantages of PCCAs. First, the nanoscale diameter of the PCCA enables extravasation of agents into tissue either through cavitation-produced inter-endothelial pores or through the leaky vessel wall in tumors via the enhanced permeability and retention effect (Ho and Yeh 2017, Ho, et al. 2016, Kang, et al. 2014, Maeda, et al. 2000, Thakkar, et al. 2013). Thus, one potentially promising application of PCCAs is for monitoring tumors (Rojas and Dayton 2019a, Williams, et al. 2013) or combined imaging and therapeutics (Fix, et al. 2019, Ho and Yeh 2017, Ho, et al. 2016). Second, the circulation life of the low-boiling point PCCA is longer than its precursor microbubbles (Sheeran, et al. 2015). This advantage could potentially provide more opportunities for targeted binding, extravasation, and sonoporation in both imaging and therapeutic applications. In addition, PCCA imaging in the local region of cardiac infarct (Choudhury, et al. 2018) and draining into lymph nodes has also been demonstrated (Yang, et al. 2017, Yoon, et al. 2017).

Several techniques have been used for imaging PCCAs. Since the PCCAs vaporize into gaseous core microbubbles, non-linear ultrasound imaging techniques such as pulse inversion have been used for PCCA imaging (Sheeran, et al. 2015). However, as in microbubble imaging, background signals from the skin and other tissue interfaces still produce echogenic artifacts. In order to reduce tissue background and further enhance image contrast, an alternative strategy is differential imaging, in which the pre-activation image is subtracted from the post-activation image (Lin, et al. 2018, Yoon and Emelianov 2018). However, this differential imaging technique is prone to low image quality in cases of high tissue motion such as respiration and cardiac motion. Another PCCA imaging technique proposed recently is vaporization detection imaging, in which low frequency oscillations of PCCAs during vaporization are used to form a high contrast image (Rojas and Dayton 2019b, Sheeran, et al. 2013). The main disadvantage of this technique is the poor spatial resolution relative to other techniques. Furthermore, ultrafast Doppler imaging techniques have been successfully demonstrated for visualizing microvasculature with high contrast by utilizing the temporal variation of flowing contrast agents in a given spatial location (Couture, et al. 2009, Errico, et al. 2016, Errico, et al. 2015). However, it would be

challenging to use this ultrafast Doppler strategy for imaging PCCAs in extravascular non-flow conditions, as the contrast agent is distinguished from tissue on the basis of variation in signal over time due to blood flow. To enable extravascular imaging and image-guided delivery with PCCAs, an imaging technique capable of visualizing a low concentration of localized, non-flowing PCCAs in the presence of significant physiological motion is needed.

In the present study, we propose to use an ultrafast inter-frame activation strategy to provide high contrast PCCA images by rapidly producing vaporization events and imaging this high-frequency fluctuation of the blinking PCCAs with high frame rate (e.g. 2000 fps) imaging interleaved between activation pulses. To produce a region of localized vaporization of PCCAs, dynamically steered, focused beams, are inserted within adjacent ultrafast imaging frames to activate PCCAs. A high pass filter is used to remove clutter signal from moving tissues and retain the signal arising from PCCA vaporization between adjacent ultrafast acquisitions. A correlation-based strategy (Huang, et al. 2018) is used to estimate PCCA signal intensity, suppress non-correlated noise, and then form the final image. Recently a super-resolution imaging technique, AWSALM, was presented which utilized interleaved activation and imaging pulses to image phase change contrast agents in tubes (Zhang, et al. 2018). In the presented ultrafast inter-frame activation ultrasound (UIAU) technique, the imaging frame rate is increased to 2000 frames per second (fps) from 100 fps in AWSALM. For the goal of imaging local activation of extravascular PCCAs, the increase in slow time samples by a factor of 20 enables a temporal resolution below 0.1 second for PCCA imaging with an ensemble length of 100 to 200 frames, which would be beneficial in high-motion rate imaging such as cardiac imaging, in which an entire cycle of cardiac motion occurs every 0.5 to 1 second. Moreover, given a 2000 Hz sampling rate in slow time, a high-cutoff frequency (900 Hz) clutter filter can be used in UIAU to suppress tissue signals including the microvascular flow signal, which is retained by a singular value decomposition (SVD) clutter filter in AWSALM and useful in microvascular imaging, but undesirable in extravascular or targeted imaging applications. These authors have also recently presented a super-resolution imaging technique based on an ultrafast imaging strategy (Zhang, et al. 2019) tested in a mimimally-attenuating water tank. Unfocused imaging pulses were used for both activating and imaging the PCCAs without additional interframe activation pulses. However, the use of unfocused pulses, which drastically decreased the acoustic pressure at depth, would decrease the ability to vaporize PCCAs at depth and increase the risk of tissue heating in the region near the transducer in the presence of tissue attenuation encountered in vivo. Moreover, there is also risk of mechanical damage to tissue in regions close to the transducer, as a mechanical index of 1.9, the safety limit regulated by Food and Drug Administration (FDA), could be reached in shallow regions. Additionally, the presented approach with interframe activation using focused waves provides an advantage over the unfocused wave in localizing PCCA vaporization, which is required in image-guided localized therapy such as blood-brain barrier opening (Chen, et al. 2013).

In the present study, the developed technique for localized activation and imaging of PCCAs in the presence of significant physiological motion was evaluated using PCCAs with decafluorobutane (DFB) cores synthesized in the lab. The performance of the UIAU technique in distinguishing between vaporized PCCAs and background tissue was evaluated in a tissue-mimicking phantom with a channel containing PCCAs and compared with pulse

inversion and differential imaging in terms of the contrast-to-tissue ratio (CTR). Tissue motion was induced at low (1 mm/s) and high (20 mm/s) speeds to test robustness of the imaging technique to physiological tissue motion. Furthermore, the in vivo imaging capability of UIAU was demonstrated by imaging PCCA vaporization in the rat liver. Finally, the imaging capability at depth of UIAU was demonstrated and compared with amplitude modulation pulse inversion imaging.

Materials and Methods:

Imaging sequence:

Imaging and activation of PCCAs were achieved by using a programmable ultrasound scanner (Vantage 256, Verasonics, Kirkland, WA, USA) with a 128-element linear array transducer (L11–5, ATL, Bothell, WA, USA).

Ultrafast inter-frame activation ultrasound (UIAU) imaging: The UIAU sequence was composed of ultrafast ultrasound imaging events interleaved with PCCA activation pulses, with one activation pulse for every 3 imaging pulses as illustrated in Figure 1. 3 unfocused 5 MHz single-cycle pulses were consecutively transmitted at 3 angles (−10°, 0° and 10°) and the echoes were received by the linear array. The time interval between the 3 imaging pulses was 100 microseconds. For these 3 steered, unfocused transmits, 3 sets of ultrasound in-phase/quadrature (IQ) baseband data were obtained after beamforming and IQ modulation. The free field peak negative pressure for the unfocused 5 MHz transmit event was measured by calibrated hydrophone to be 370 kPa (Mechanical index, MI = 0.17).

To activate the PCCAs, focused 5 MHz, 3-cycle pulses were transmitted using the full aperture of the array. By changing the transmitting delays along the array, the beam can be focused at different locations to locally activate the PCCAs. Based on acoustic measurements in free field, the peak negative pressures derated by 0.3 dB/(cm·MHz) were 3.04 MPa (MI = 1.36) at 10 mm and 3.49 MPa (MI = 1.56) at 15 mm. Assuming an attenuation of 0.42 dB/(cm*$MHz^{1.21}$) in the rat liver at 5 MHz (Tuthill, et al. 1989), the pressures were 2.57 MPa at 10 mm and 2.72 MPa at 15 mm. The focused activation pulse was transmitted 50 microseconds after the third imaging pulse. Transmitting for the next group of imaging pulses began 250 microseconds after the previous activation pulse. The time interval between 2 adjacent packets of imaging and activating pulses was 500 microseconds, which resulted in a 2000 Hz sampling rate (i.e., the acquisition rate in “slow time”). To activate the PCCA at multiple locations within the field of view, an ensemble of multiple sets of imaging and activating pulses were applied. In this study, an ensemble size of 196 was used to achieve 196 PCCA vaporization events within the field of view. The total time required was less than 0.1 second (i.e., 196 × 500 microseconds).

In the slow-time domain where ultrasound frames were acquired at 2000 Hz, the activation of PCCAs produces a sudden change in pixel intensity, which is a step function signal (Figure 2K) in slow time, while the motion of tissue clutter produces a low frequency, sinusoidally-varying signal in slow time. In order to remove low frequency tissue signal and retain the high frequency signal from the activation of PCCAs, the 3 sets of 196 acquisitions of IQ data were filtered pixel-wise in the slow time domain using an 8th-order high pass

clutter filter (40 dB attenuation at 900 Hz). Instead of estimating the PCCA signal intensity using the conventional zero-lag auto-correlation, a cross-correlation strategy was used. This strategy has been demonstrated for suppression of non-correlated background noise and sidelobe artifacts for microvascular Doppler imaging (Huang, et al. 2018). Specifically, the filtered IQ data from the −10° and 10° transmit events were coherently compounded. Then, the correlation value of each pixel was obtained by calculating the mean of the pixel-wise product of the 2-angle-compounded IQ data and the 0° IQ data. The final UIAU image was obtained by taking the square root of the real part of the correlation value at each pixel.

Pulse inversion imaging: Pulse inversion images were formed by summing the IQ data obtained after sequentially transmitting one positive pulse and one negative pulse. 4.5 MHz single-cycle pulses were used to maximize the harmonic components in the transducer bandwidth, as in previous studies of PCCA imaging (Rojas and Dayton 2016). No additional digital filtering was applied, as additional filtering did not yield significant improvement in CTR for PCCA imaging in preliminary tests. A single pulse inversion frame was obtained by coherent compounding of IQ data from 3 steered, unfocused beam transmits. The steering angles were the same as in the UIAU sequence. The free field maximum peak negative pressure of the unfocused 4.5 MHz beam was 357 kPa (MI = 0.17). In pulse inversion mode, 196 activation beams, which were the same as that in UIAU sequence, are transmitted immediately after the acquisition of the pre-activation pulse inversion image. Post-activation pulse inversion images were acquired immediately following activation pulses. The pulse repetition rate of the activation pulses was 20 kHz, which is 10 times higher than that in UIAU sequence. Therefore, the time interval between the pre-activation and the post-activation acquisitions was about 0.01 seconds (i.e., 196 × 50 microseconds).

Differential imaging: Pre-activation and post-activation B-mode images were acquired simultaneously during the acquisition of the pulse inversion images. That is, the differential image was obtained by subtracting the pre-activation B-mode IQ data from the post-activation data.

Synthesis and sizing of phase change contrast agent

Lipid solutions were formulated as previously described (Lindsey, et al. 2017) using a 9:1 molar ratio of 1,2-distearoyl-sn-glycero-3-phosphocholine (DSPC) and 1,2-distearoyl-sn-glycero-3-phosphoethanolamine-N-methoxy (polyethylene–glycol)-2000 (DSPE-PEG2000) (Avanti Polar Lipids, Alabaster, AL) in a solution containing propylene glycol 15% (v/v), glycerol 5% (v/v), and phosphate-buffered saline (PBS) 80% (v/v). 1.5 mL of lipid solution were placed in sealed 3 mL glass vials and the air headspace was exchanged with decafluorobutane (DFB, boiling point: −2° C) gas (Fluoromed, Round Rock, TX, USA). Microbubbles with DFB gas cores and phospholipid shells were formed by agitation in a Vialmix device (Lantheus Medical Imaging, N. Billerica, MA). Phase change contrast agents were synthesized by condensing lipid-shelled microbubbles in an isopropanol bath maintained at −10° C by dry ice. 20 ml of air was pushed into the vial using a ratcheting syringe to provide additional pressure. DFB-core PCCAs are more stable than low-boiling-point perfluorocarbon agents with octafluoropropane cores (OFP, boiling point: −37° C) (Sheeran, et al. 2015), and thus are more suitable for imaging at body temperature. The size

distribution of the PCCA was measured using a NanoSight NS300 (Malvern Instruments, Westborough, MA, USA). Before measuring, the PCCA solution was diluted by a factor of 200.

Phantom studies

A custom tissue-mimicking phantom was developed consisting of gelatin (0.06 g/ml), agar (0.005 g/ml), 1-propanol (5% V/V), glutaraldehyde (1.2% V/V) and water (93.8% V/V). Graphite powder (0.06 g/ml) was added into the phantom to produce acoustic scattering. The attenuation coefficient of the phantom is approximately 2.8 dB/cm at 5 MHz. Agar and glutaraldehyde were added to prevent the phantom from melting at 37° C during experiment (Madsen, et al. 1978). A 5 mm-diameter channel located approximately 7 mm below the surface was created inside the phantom. To ensure sufficient space for the transducer to move axially, the linear array was placed 3 mm above the phantom. Therefore, the center of the channel was located approximately 10 mm deep.

First, PCCA images were acquired using the phantom without motion. The foci of the activation beams were separated by 0.5 mm in both the axial and lateral, as similar to that in the previous research (Rojas and Dayton 2016), in which the same transducer model was used to activate PCCAs, although the activation pressure matching approach (Rojas and Dayton 2016) was not used in the present study. Moreover, the foci spacing and the activation region were also determined by the dimension of the phantom channel. The activation region was a 14 × 14 grid of the foci of the 196 activation beams, which was large enough (6.5 × 6.5 mm^2 starting at a depth of 7 mm) to cover the phantom channel (Figure 2A). The −6 dB width of the activation region for this transducer at 5 MHz is estimated from the UIAU image. At a depth of 10 mm in the phantom channel, for the given acoustic output pressure and the configuration of the unfocused imaging wave, the widest −6 dB activation region covers approximately 0.52 mm, i.e. 2 pixels, on the lateral direction. The PCCA solution was diluted by a factor of 400 and warmed up to 37° C in a water bath before infusion into the phantom channel. The concentration of the nanodroplets is approximately 10^8 particles/ml according to the size distribution measurements of PCCAs. Prior to infusion of the PCCA solution into the phantom channel, baseline images were acquired using the UIAU sequence (Figure 2B) and pulse inversion (Figure 2E). During infusion into the phantom channel, PCCAs were observed to cool slightly to approximately 35° C as measured by a digital thermometer during preliminary testing of the setup. After the PCCA solution was infused and the flow was stopped, the pre-activation images were acquired immediately by using either pulse inversion imaging (Figure 2F) or UIAU without activation pulses (Figure 2C). Then, activation pulses were enabled and the UIAU image of the activated PCCA was acquired by using the UIAU sequence (Figure 2D). Following the 20 kHz activation pulses, the post-activation pulse inversion image (Figure 2G) was also acquired with PCCAs in the phantom channel. Before each acquisition, the phantom channel was flushed using degassed warm water for at least 30 seconds and fresh PCCA solution was then infused into the channel.

Next, the three imaging strategies were investigated in the phantom with motion introduced in 3 directions (i.e., axial, lateral and elevational directions with respect to the imaging plane

of the linear array). The 3 motion directions are illustrated in Figure 2A. Two motion rates were investigated in this study: 1 mm/s and 20 mm/s. The higher motion rate at 20 mm/s was introduced to simulate motion that occurs during peak respiratory motion (Seppenwoolde, et al. 2002). The 1 mm/s motion was introduced to test the performance of differential imaging at a much lower motion rate, i.e. similar to that during the minimum velocity phase of respiration. Instead of directly moving the phantom, simulation of tissue motion was achieved by moving the ultrasound transducer mounted on a 3-axis motion stage (XPS-Q8, Newport, Irvine, CA, USA). The motion stage controller was programmed to send a trigger signal to the ultrasound scanner to start imaging when the programmed velocity is achieved.

For imaging in the presence of motion in phantoms, the axial and lateral spacing between the foci of the activation beams was increased to 0.8 mm. The activation region was a 14 × 14 matrix of 196 foci of the activation beams and was large enough (10.4 × 10.4 mm^2 starting at 7 mm deep) to ensure that the phantom channel would not move outside of this activation region during the simulated motion.

The contrast-to-tissue ratio (CTR) was calculated to evaluate the performance of these imaging techniques for distinguishing the PCCA-filled channel from the tissue-mimicking background. The contrast (PCCA) signal magnitude was obtained by averaging the signal magnitude inside the region in the channel indicated by the red rectangle, while the tissue signal magnitude was obtained by averaging the signal magnitude in the region surrounding the phantom channel indicated by the white rectangles (Figure 2E). The contrast signal magnitude (i.e., S_{PCCA}) and tissue signal magnitude (i.e., S_{Tissue}) were used to calculate the CTR: i.e. $CTR = 20 \times log_{10}(S_{PCCA}/S_{Tissue})$. The regions used for CTR calculations were separated by 1.3 mm and 2.6 mm in the axial and lateral directions, respectively. Contrast enhancement (i.e., ratio between the pre-activation baseline signal intensity and the post-activation signal intensity in the region of interest), which has been used in previous studies on PCCA imaging (Sheeran, et al. 2015), was not used here since there were no acoustic scatterers inside the phantom channel before the activation of PCCAs.

In vivo demonstration of UIAU imaging

To demonstrate the feasibility and performance of UIAU for in vivo imaging, two 5–6 week-old male Sprague-Dawley rats (Envigo, Greenfield, IN, USA) were imaged according to a protocol approved by the Institutional Animal Care and Use Committee of Emory University. The rats were anesthetized using 2.5% isoflurane and placed on a heating pad. Real-time B-mode imaging was used to monitor respiration. The respiration rate was approximately 60 breaths per minute, i.e. 1 Hz.

Before injection of PCCAs, baseline images were acquired using UIAU, pulse inversion and differential imaging techniques for each rat during either minimum respiratory motion or peak respiratory motion. Next, PCCA solution was injected via tail vein at a concentration 33 microliters per 100 grams of body weight (total concentration 4.0×10^{10} particles/ml) for each rat. 2 minutes after injection, images were acquired using either pulse inversion or UIAU sequence. Differential images were also acquired during the acquisition of pre-activation and post-activation pulse inversion images. The pre-activation UIAU image was

acquired using UIAU with the PCCA activation pulses disabled. Immediately after the acquisition of the pre-activation UIAU image, the UIAU image of PCCAs was acquired by enabling the PCCA activation pulses. The spacing between 196 activation beam foci is 0.8 mm for all 3 imaging techniques. Preliminary results indicated that there is no contrast enhancement after >24 hours of waiting. Therefore, when the same animal was imaged more than once, PCCAs were allowed to clear out of rat tissue by waiting >24 hours. For in vivo imaging, the contrast enhancement was calculated for each imaging technique as the ratio of signal magnitudes between the post-activation PCCA image and the baseline image.

Imaging at depth

To test imaging capability at depth, a layer of 15 mm thick porcine liver was placed on the top of the tissue-mimicking phantom. The attenuation of the excised porcine liver is approximately 4.5 dB/cm at 5 MHz (Bush, et al. 1993). The phantom channel containing contrast agents was located > 25 mm deep below the ultrasound transducer.

In order to ensure sufficient CTR at depth, a 3-pulse amplitude modulation pulse inversion (AMPI) sequence with 17 steered transmit events at varying angles (−10° to 10°) was used here (Couture, et al. 2012). Thus the total number of transmit events was 51 (3 pulses per angle: 1 full-amplitude pulse and 2 inverted half-amplitude pulses). Baseline images were acquired in the absence of the PCCA. The post-activation AMPI image was acquired after 196 focused beams were transmitted to vaporize the PCCAs in the phantom channel. The baseline and post-activation UIAU images were also acquired.

The driving voltage of the transducer was increased to 40 V in order to achieve vaporization of contrast agents at depth. The focused beam for activating contrast agents was not directly measured in non-attenuating free field to prevent potential damage to the hydrophone. For the unfocused imaging wave, with the attenuation induced by the 10 mm phantom and 15 mm excised liver, peak negative pressure of the 5 MHz unfocused wave in the UIAU sequence was estimated to be 258 kPa (MI = 0.12) based on acoustic measurements. The peak negative pressure of the full amplitude 4.5 MHz unfocused wave in amplitude modulation pulse inversion was 286 kPa (MI = 0.14).

Results:

Size distribution of the PCCAs

Five recordings of 60 seconds in length of diluted DFB-core PCCAs yielded mean and mode diameters of 161.2 nm and 127.1 nm, respectively, with a standard deviation of 65.1 nm and a concentration of $2.01\times10^{8} \pm 3.17\times10^{6}$ particles/ml. According to these measurements, the concentration of the PCCAs in the phantom study was approximately 10^{8} particles/ml.

Imaging PCCA activation in a stationary phantom

In the pulse inversion baseline and pre-activation images (Figure 2E and F), the anechoic channel was distinguishable from the surrounding echogenic gel-phantom. Conversely, the channel was not discernable in the baseline UIAU (Figure 2B), pre-activation (Figure 2C) UIAU, or baseline differential images (Figure 2H). In the post-activation pulse inversion

image (Figure 2G), the vaporization of the PCCAs resulted in the channel being filled up with echogenic, speckle-producing targets. However, it was difficult to distinguish the vaporized PCCAs from the surrounding tissue in this image (Figure 2G) to determine the locations of PCCA vaporization.

In the UIAU (Figure 2D) and differential (Figure 2I) images of PCCAs activated by 196 focused beams, the channel became hyperechoic. Although most of the surrounding tissue remained anechoic, there were some echogenic speckle-producing targets located immediately deep to the hyperechoic channel in the differential image (Figure 2I), while some weak signals originated from near the bottom of the UIAU image (Figure 2D). The enhancement distal to the channel might be due to reduced attenuation through the phantom channel compared with the surrounding background. The variation of the B-mode signal intensity of the pixel in the center of the phantom channel over the entire ensemble length (196 frames) is also illustrated in Figure 2K. The activation of PCCAs formed a step function. Overall, the PCCA vaporization in the channel was easy to distinguish from the surrounding tissue background using UIAU.

The CTR was obtained from the PCCA images (Figure 2D, G and I) for these 3 imaging techniques. 5 measurements from 5 independent acquisitions were made for each technique. The CTR of UIAU, pulse inversion and differential images were 17.3±0.9 dB, 2.1±1.4 dB and 22.6±3.5 dB respectively (Figure 2J). Mann-Whitney U-test indicated that UIAU produced a significantly higher CTR than that of pulse inversion ($p < 0.01$). However, UIAU did not perform any better than differential imaging.

Imaging PCCAs in a phantom with motion

Figure 3 shows the images of PCCAs in the phantom channel when the linear array was translated in 3 orthogonal directions at a low speed (1 mm/s). The focused activating beams with 0.8 mm spacing resulted in a set of uniformly-spaced, hyperechoic targets within the phantom channel. In the UIAU images (the first row of Figure 3), the gel-phantom surrounding the channel exhibited low intensity compared with the hyperechoic region filled with PCCAs. In the pulse inversion images (the second row of Figure 3), there was still high image intensity in the region of the tissue-mimicking phantom surrounding the channel resulting from poor cancelation. For differential imaging, the region in the phantom outside the channel was echogenic when the motion was along the axial direction (Figure 3G), although the image intensity in this region was much lower compared with the region of PCCA activation in Figure 3H and 3I. In addition, the phantom-water interface, as indicated by the white arrows in Figure 3H and 3I, was still discernible in the differential images while it was not visible in the UIAU images.

Figure 4 shows the images acquired from the same phantom at a higher motion rate (i.e., 20 mm/s). In the UIAU images, the magnitudes of signals from the surrounding phantom were still quite low compared with the region of PCCA activation in the channel. In the pulse inversion images (the second row of Figure 4), the image intensity in the gel phantom appeared to be similar to that of the activated PCCAs, although there were visible echoes at the bottom of the channel in Figure 4D. The results of differential imaging (the third row of Figure 4) showed significant non-cancelation of signals in the gel of the phantom. There is

visible variation of the background brightness between the different motion directions, which could be due to strong echoes at the top and bottom of the channel that fail to cancel in the presence of motion, or due to hyperechoic contrast agents that aggregate at the bottom of the channel even though the channel was flushed using degassed water for more than 30 seconds before each acquisition. Therefore, during the quantification of the CTR, the ROI is always placed inside the channel and the channel wall was not included.

Quantitative evaluation of CTR values are shown in Figure 5. At 1 mm/s, the CTRs for UIAU images were 13.1±0.8 dB, 12.1±0.8 dB, and 12.9± 0.7 dB for axial, lateral, and elevational motion respectively, while the CTRs for pulse inversion were −2.0±1.0 dB, −0.9±1.3 dB, and −1.1±1.2 dB, and the CTRs for differential imaging were 3.5±1.6 dB, 9.7±6.4 dB, and 13.75±4.9 dB (Figure 5A). The Mann-Whitney U-test indicated that the CTR of UIAU and differential imaging were both significantly higher than pulse inversion imaging ($p<0.01$). However, UIAU didn't perform any better than differential imaging for motion in the lateral and elevation directions.

At 20 mm/s, the CTRs for UIAU image were 16.1±1.0 dB, 12.8±1.1 dB, and 13.7±0.9 dB for axial, lateral, and elevational motion, respectively, while the CTRs for pulse inversion were 3.4±1.4 dB, −0.5±1.5 dB, and −1.4±0.5 dB and the CTRs for differential imaging were 3.9±2.3 dB, −0.8±1.9 dB, and 3.9±1.6 dB (Figure 5B). The CTR of UIAU is significantly higher than both pulse inversion and differential imaging at 20 mm/s ($p<0.01$).

In vivo demonstration

The B-mode, pulse inversion, and differential images of the rat liver were acquired simultaneously during the low velocity phase of respiratory motion (Figure 6). In B-mode imaging (Figure 6A), the liver appeared hypoechoic compared with the hyperechoic stomach and small intestine located below the liver. The overlapped region between the liver and the activation beam foci were indicated by the green border. When the post-activation pulse inversion image (Figure 6D) was compared with the baseline (Figure 6B) and pre-activation images (Figure 6C), it can be seen that the 196 activation beams resulted in a set of uniformly-spaced hyperechoic activation regions in the liver. The signal magnitude (normalized to the baseline signal magnitude) of the pre-activation image (Figure 6C) in the activation region (indicated by the green border in Figure 6A) was 1.4 dB, while the signal magnitude of the post-activation (Figure 6D) image was 7.3 dB. However, the clutter signal (signal magnitude at 4.6 dB in Figure 6D) in the region indicated by the yellow rectangle, which was not within the activation regions (indicated by the red dots), remained as echogenic as the vaporized PCCAs through Figure 6B to 6D. These targets were highly likely the echogenic tissues rather than the vaporized PCCAs. Thus it was difficult to differentiate between PCCAs and the tissue clutter signals in pulse inversion images. Most of the tissue signal appeared anechoic in the baseline differential image acquired without PCCA injection except for a small number of hyperechoic targets (Figure 6E), compared with the post-injection differential image (Figure 6F) of the PCCAs, although there was still some echogenic signal outside the activation region in Figure 6F. The PCCA signal magnitude in the activation region in Figure 6F was 21.1 dB, while the amplitude of the clutter signal was 13.7 dB.

The same images were also acquired during the peak velocity of the respiration phase (Figure 7). The vaporized PCCAs were again echogenic speckles (5.9 dB) in the hypoechoic liver in the post-activation pulse inversion image (Figure 7D) compared with baseline (Figure 7B) and pre-activation (Figure 7C) images. In all these pulse inversion images, the skin can be identified as echogenic layers (indicated by the white arrows) superficial to the hypoechoic liver. The amplitude of the clutter signal in the yellow-bounded region in Figure 7D was 6.9 dB, which was similar to the amplitude of the PCCA signal. Again, it was not possible to distinguish between the vaporized PCCAs using the post-activation pulse inversion image alone. In the baseline differential image (Figure 7E) acquired before injection, the liver deep to the echogenic skin exhibited higher image intensity compared with the B-mode and pulse inversion images. The vaporized PCCAs appeared as bright, hyperechoic targets in the differential image (Figure 7F). However, the signal magnitude of the region of PCCA activation was only 0.6 dB when it was normalized to the baseline. Part of the skin layer and the tissue outside the activation region still appeared echogenic in Figure 7F. It was also difficult to distinguish between the vaporized PCCAs and the tissue in the differential image.

The UIAU images were acquired during minimum respiratory motion (Figure 8) and peak respiratory motion (Figure 9) in the rats. The echogenic tissue (in the yellow bounded region) outside the activation region in the B-mode images (Figure 8A and Figure 9A) became anechoic in the baseline and pre-activation UIAU images (Figure 8B, C and Figure 9B, C). As the PCCA activation pulses were applied, these dark regions in the field of view were illuminated by the uniformly spaced echogenic targets, while the region outside the activation beam foci remained dark (Figure 8D and 9D). During minimum respiratory motion, the magnitudes of the pre-activation (Figure 8C) and the tissue clutter signal in Figure 8D were 0.2 dB and 0.1 dB, respectively, while that of the PCCA signal (Figure 8D) was 19.5 dB. During peak respiratory motion, the magnitudes of the pre-activation (Figure 9C) and tissue clutter signals in Figure 9D were 0.01 dB and −1.0 dB respectively, while that of the PCCA signal (Figure 9D) was 12.3 dB.

Overall, results indicate a contrast enhancement of 15.9±5.0 dB for UIAU, while the contrast enhancements for pulse inversion and differential imaging were 6.6±1.0 dB and 10.9±14.5 dB, respectively. Importantly, as shown in the color-coded UIAU image overlaid on grayscale B-mode images (Figure 8E and 9E), the PCCAs vaporized in the confined region could be easily located and distinguished from the background tissue at both low and high rates of respiratory motion.

Imaging at depth

The amplitudes of focused beams were adjusted to be higher than the vaporization threshold of the DFB droplets until significant contrast enhancement was seen in the post-activation amplitude modulation pulse inversion image (Figure 10B). The baseline and post-activation UIAU images using the same focused activation beams were shown in Figure 10. The CTR, which was measured in the post-activation images, indicated that the UIAU sequence (CTR = 27.8±0.9 dB) provides significantly higher contrast than AMPI (CTR = 11.9±0.9 dB) at a

depth > 25 mm. The increased CTR of UIAU, which was significantly higher than the CTR at shallow region (Figure 2), is due to the increased driving voltage and acoustic pressure.

Discussion:

The phantom study results indicated that the proposed UIAU imaging technique performs better than pulse inversion in all cases. The differential imaging performed the best when there was no tissue motion (Figure 2J), but its performance degraded (Figure 5) when motion was introduced, especially when a high motion rate (i.e., 20 mm/s) was introduced to mimic breath motion. It was also found that the CTR for pulse inversion in the presence of axial motion at 1 mm/s was −2.0±1.0 dB, and at 20 mm/s was 3.4 ±1.4 dB. Similarly, UIAU performs better at 20 mm/s than that at 1 mm/s. While there is expected to be variation between acquisitions (i.e. due to local variation of contrast agents), pulse inversion and differential imaging were compared in the same experimental setup using contrast agents from the same preparation at each motion direction and motion rate. Except for the 20 mm/s axial motion case, there was no significant difference in the CTR of UIAU between high and low motion rate as indicated by Kruskal-Wallis test combined with a pairwise comparison. Collectively, these results indicated that the UIAU provides a higher contrast than the pulse inversion.

The CTR of pulse inversion PCCA images was quite low in the phantom study even when the activation foci were dense enough to fill the phantom channel with vaporized PCCAs (Figure 2G). To ensure the performance of the pulse inversion sequence, the precursor DFB microbubbles (diluted by a factor of 4000, i.e. 10^7 bubbles/ml) were also imaged in the phantom with the same pulse inversion imaging sequence used in PCCA imaging. Both single-pulse B-mode and pulse inversion images of the DFB microbubbles are shown in the supplemental figure. 21.6±0.1 dB suppression of the graphite phantom signal was achieved with pulse inversion, resulting in a CTR of 12.4±0.8 dB with microbubbles alone, which is much higher than that of PCCAs. This is consistent with previous reports that the contrast of precursor microbubbles (12.63±3.64 dB in Sheeran, et al. 2015) is higher than the vaporized PCCAs (7.29 ± 3.65 dB in Sheeran, et al. 2015). The difference in CTR between the vaporized PCCA and the precursor microbubble images could be due to the focused activation pulses, as a large portion of vaporized PCCAs were excessively insonified and, therefore, potentially destroyed by the focused pulses. Another cause for this difference could be the difference in acoustic behavior between the vaporized PCCA and the precursor microbubbles, which has been previously reported (Lin, et al. 2018). It should be also noted that the level of tissue suppression in contrast-specific imaging sequences is highly dependent on the hardware, i.e. the degree of cancellation of pulses produced by the transmit circuitry and transducer.

For pulse inversion imaging results, there were also differences between the in vivo contrast enhancement measurements (6.6±1.0 dB) and the CTR values measured in the phantom. This is likely due to differences in the acoustic scattering property between the graphite phantom and the liver, though the nature of the motion is also different in vivo. The same acoustic output was used for in vivo and phantom studies, but the rat liver was less echoic than the phantom, which would be expected to produce higher in vivo contrast enhancement

measurements. Despite this, the in vivo contrast enhancement measured in this study is similar to the contrast enhancement reported in a previous study (7.29 ± 3.65 dB) using the same type of contrast agents (Sheeran, et al. 2015).

The final UIAU image was obtained by compounding 196 ultrafast frames acquired at 2000 frames per second (fps). While low-cutoff frequency clutter filters can be used for filtering tissue motion and spatiotemporal SVD filters have been demonstrated for suppressing tissue clutter while retaining low-flow rate microvascular signals that are otherwise inseparable from moving tissue in the frequency domain, in this case a high-cutoff frequency (900 Hz) clutter filter was used to suppress tissue signals including the microvascular flow signal in order to image agents with very low motion in the presence of high tissue motion, as in extravascular or molecular-targeted imaging applications. Using a center frequency of 5 MHz and a slow-time sampling frequency of 2000 Hz results in Doppler aliasing at speeds of 150 mm/s. The 900 Hz cutoff frequency provides cutoff velocity at 135 mm/s, which makes the high frequency signal of PCCAs separable from most moving tissues, as tissue motion including respiratory motion is normally much slower than 135 mm/s. However, the peak cardiac tissue velocity could be higher than 135 mm/s. Therefore, a higher imaging frame rate might be required for cardiac imaging applications. Alternatively, since the PCCA activation observed in successive acquisitions is a step function compared with the sinusoidally-varying tissue signal, an alternative clutter filtering strategy might be employed to improve separation between tissue motion and PCCA activation in order to form an image of PCCA activation alone.

Another factor that could affect the UIAU image quality is random noise. Denoising would be particularly helpful for low concentration and higher frame rate imaging scenarios, when even fewer angles of unfocused imaging pulses can be utilized. Although the correlation strategy used in the present study has been demonstrated to significantly decrease background noise level, there is still room to further improve the signal to noise ratio by employing additional filtering and signal processing strategies. For instance, SVD filters could potentially be used to suppress the spatially uncorrelated random noise by rejecting the last few high-order singular values in addition to high-pass filtering to cancel tissue signals.

CTR values in UIAU images were higher in the stationary phantom than in the case of induced tissue motion, likely due to the PCCAs being activated with a higher spatial density in the stationary phantom. A high density of activation could be achieved by shrinking the activation area or increasing the number of activation pulses. To maintain a constant activation area and imaging speed, a higher pulse repetition frequency is needed. In the present study, the pulse repetition frequency of the activation beams is 2000 Hz, which is the same as the ultrafast imaging frame rate since there is only one activation pulse between adjacent imaging frames. Denser activation foci are achievable by inserting 2 or more activation pulses between the imaging frames. These tradeoffs will likely be determined based on the rate of local physiological motion for the intended application.

Deeper imaging depth is achievable by increasing the focal depth and pressure of the focused activation beams as shown in Figure 10 and the previous study (Rojas and Dayton

2019b). Besides, activation pulses at lower frequencies with increased penetration and increased mechanical index would also favor the vaporization of PCCAs in the deep imaging scenario. To activate PCCAs in both shallow and deep tissues without damaging the tissue in shallow regions, a uniform acoustic pressure within the FDA limit across a large depth range is desired (Rojas and Dayton 2016). However, one limitation of the present UIAU sequence is that a uniform acoustic pressure across a large depth range is difficult to achieve, as this would require rapidly changing the transducer driving voltage, as indicated by previous research (Rojas and Dayton 2016). An alternative option for imaging activation in tissue across a large range of depths could be to run the UIAU sequence multiple times with different voltage levels at different depths. Simultaneous generation of multiple foci has also been demonstrated (Ebbini and Cain 1989, Ilovitsh, et al. 2019, Matrone, et al. 2017, Song, et al. 2012), which could facilitate the generation of larger activation areas with increased imaging rates. In addition, presented images were processed offline in this study, with the image formation process requiring several minutes, which is much longer than the data acquisition time (i.e. < 0.1 s). However, implementation of this pixel-by-pixel processing algorithm in a parallel manner on a graphics processing unit could potentially enable real-time image formation.

In potential applications such as extravascular imaging and delivery, the vaporization of PCCAs could be detected and used as an indicator of molecular binding (Rojas and Dayton 2019a), extravasation within a tumor (Williams, et al. 2013) or local aggregation in an infarct zone (Choudhury, et al. 2018). UIAU is a strong candidate to cancel tissue signal and retain the PCCA signal in these applications. However, stationary targeted or extravasated agents would need to be differentiated from the non-targeted circulating agents. A potential solution is to acquire UIAU images after a sufficient wait time for the free flowing PCCAs to be cleared out of the circulation while the targeted and extravasated PCCAs remain stable before activation by ultrasound. A previous study of extravascular imaging in mice with KHT-C sarcoma tumors suggests a waiting time of 1.5 hours for differentiating tumor and healthy tissue (Williams, et al. 2013). However, these times would likely depend on pathophysiology as well as the core gas of the PCCA, thus additional studies are still needed to determine the optimal wait time for the DFB-core PCCA used in the present study for a given application.

Finally, while PCCA activation in these feasibility studies was performed using focal locations in a grid with uniform spacing in order to assess the robustness of imaging techniques to physiological motion, in the future, the UIAU approach could be used to selectively activate PCCAs in small, well-defined locations. The UIAU image could then be overlaid on the B-mode image (as in Figures 8D and 9D) to allow tracking of activation locations, e.g. for live tracking of local therapeutic delivery in the presence of physiological motion.

Conclusion:

The results of the phantom study indicate the proposed UIAU imaging technique provides a significantly higher contrast-to-tissue ratio for PCCA imaging relative to conventional pulse inversion imaging. Although the differential imaging strategy performs the best in the

absence of motion, its performance degrades with tissue motion, as indicated by the results of the phantom study. The UIAU technique is more robust to tissue motion, especially at higher velocities. In addition, the proposed UIAU technique also provides higher CTR than that of the amplitude modulation pulse inversion (AMPI) approach for PCCA imaging at a depth of 25 mm. The in vivo results also demonstrate the UIAU technique is able to enhance image contrast in PCCA imaging in a localized vaporization region and significantly suppress the background tissue signal in the presence of respiratory motion. Overall, the UIAU technique is a promising imaging tool for locally activating and visualizing the nanoscale PCCAs. This technique can potentially be used to further enhance the contrast of the PCCA-based extravascular imaging and targeted molecular imaging at a low concentration of PCCAs and for image-guided drug delivery.

Supplementary Material

Refer to Web version on PubMed Central for supplementary material.

Acknowledgements:

The authors thank Graham Collins and Yutong Guo for assistance with experimental preparation and thank Jesutoyosi Awoyeye for assistance with synthesizing contrast agents. This work was supported in part by the Department of Biomedical Engineering and the College of Engineering at Georgia Institute of Technology and by R01HL144714 from the National Institutes of Health.

References:

Apfel RE. 1998 Activatable infusable dispersions containing drops of a superheated liquid for methods of therapy and diagnosis. U.S. Patent No. 5,840,276.

Bez M, Foiret J, Shapiro G, Pelled G, Ferrara KW, Gazit D. Nonviral ultrasound-mediated gene delivery in small and large animal models. Nat Protoc 2019; 14:1015–26. [PubMed: 30804568]

Bush NL, Rivens I, Terhaar GR, Bamber JC. Acoustic Properties of Lesions Generated with an Ultrasound Therapy System. Ultrasound Med Biol 1993; 19:789–801. [PubMed: 8134979]

Cao Y, Chen Y, Yu T, Guo Y, Liu F, Yao Y, Li P, Wang D, Wang Z, Chen Y. Drug release from phase-changeable nanodroplets triggered by low-intensity focused ultrasound. Theranostics 2018; 8:1327–39. [PubMed: 29507623]

Chen CC, Sheeran PS, Wu SY, Olumolade OO, Dayton PA, Konofagou EE. Targeted drug delivery with focused ultrasound-induced blood-brain barrier opening using acoustically-activated nanodroplets. J Control Release 2013; 172:795–804. [PubMed: 24096019]

Choudhury SA, Xie F, Kutty S, Lof J, Stolze E, Porter TR. Selective infarct zone imaging with intravenous acoustically activated droplets. PLoS One 2018; 13:e0207486. [PubMed: 30551125]

Couture O, Bannouf S, Montaldo G, Aubry J-F, Fink M, Tanter M. Ultrafast imaging of ultrasound contrast agents. Ultrasound Med Biol 2009; 35:1908–16. [PubMed: 19699026]

Couture O, Fink M, Tanter M. Ultrasound contrast plane wave imaging. IEEE Trans Ultrason Ferroelectr Freq Control 2012; 59:2676–83. [PubMed: 23221216]

Ebbini ES, Cain CA. Multiple-Focus Ultrasound Phased-Array Pattern Synthesis - Optimal Driving-Signal Distributions for Hyperthermia. IEEE Trans Ultrason Ferroelectr Freq Control 1989; 36:540–48. [PubMed: 18290231]

Errico C, Osmanski B-F, Pezet S, Couture O, Lenkei Z, Tanter M. Transcranial functional ultrasound imaging of the brain using microbubble-enhanced ultrasensitive Doppler. Neuroimage 2016; 124:752–61. [PubMed: 26416649]

Errico C, Pierre J, Pezet S, Desailly Y, Lenkei Z, Couture O, Tanter M. Ultrafast ultrasound localization microscopy for deep super-resolution vascular imaging. Nature 2015; 527:499–502. [PubMed: 26607546]

Fix SM, Koppolu BP, Novell A, Hopkins J, Kierski TM, Zaharoff DA, Dayton PA, Papadopoulou V. Ultrasound-Stimulated Phase-Change Contrast Agents for Transepithelial Delivery of Macromolecules, Toward Gastrointestinal Drug Delivery. Ultrasound Med Biol 2019; 45:1762–76. [PubMed: 31003709]

Hannah AS, Luke GP, Emelianov SY. Blinking Phase-Change Nanocapsules Enable Background-Free Ultrasound Imaging. Theranostics 2016; 6:1866–76. [PubMed: 27570556]

Hernot S, Klibanov AL. Microbubbles in ultrasound-triggered drug and gene delivery. Adv Drug Deliver Rev 2008; 60:1153–66.

Ho Y-J, Yeh C-K. Theranostic performance of acoustic nanodroplet vaporization-generated bubbles in tumor intertissue. Theranostics 2017; 7:1477–88. [PubMed: 28529631]

Ho YJ, Chang YC, Yeh CK. Improving Nanoparticle Penetration in Tumors by Vascular Disruption with Acoustic Droplet Vaporization. Theranostics 2016; 6:392–403. [PubMed: 26909113]

Huang C, Song P, Gong P, Trzasko J, Manduca A, Chen S. 2018 Simultaneous Noise Suppression and Incoherent Artifacts Reduction In Ultrafast Ultrasound Microvessel Imaging. IEEE International Ultrasonics Symposium Kobe, Japan.

Ilovitsh A, Ilovitsh T, Foiret J, Stephens DN, Ferrara KW. Simultaneous Axial Multifocal Imaging Using a Single Acoustical Transmission: A Practical Implementation. IEEE Trans Ultrason Ferroelectr Freq Control 2019; 66:273–84. [PubMed: 30530361]

Kang S-T, Huang Y-L, Yeh C-K. Characterization of acoustic droplet vaporization for control of bubble generation under flow conditions. Ultrasound Med Biol 2014; 40:551–61. [PubMed: 24433748]

Kang ST, Lin YC, Yeh CK. Mechanical bioeffects of acoustic droplet vaporization in vessel-mimicking phantoms. Ultrason Sonochem 2014; 21:1866–74. [PubMed: 24690297]

Kripfgans OD, Fowlkes JB, Miller DL, Eldevik OP, Carson PL. Acoustic droplet vaporization for therapeutic and diagnostic applications. Ultrasound Med Biol 2000; 26:1177–89. [PubMed: 11053753]

Lin S, Shah A, Hernández-Gil J, Stanziola A, Harriss BI, Matsunaga TO, Long N, Bamber J, Tang M-X. Optically and acoustically triggerable sub-micron phase-change contrast agents for enhanced photoacoustic and ultrasound imaging. Photoacoustics 2017; 6:26–36. [PubMed: 28507898]

Lin S, Zhang G, Jamburidze A, Chee M, Leow CH, Garbin V, Tang M-X. Imaging of vaporised sub-micron phase change contrast agents with high frame rate ultrasound and optics. Phys Med Biol 2018; 63:065002. [PubMed: 29384498]

Lindsey BD, Shelton SE, Martin KH, Ozgun KA, Rojas JD, Foster FS, Dayton PA. High resolution ultrasound superharmonic perfusion imaging: In vivo feasibility and quantification of dynamic contrast-enhanced acoustic angiography. Ann Biomed Eng 2017; 45:939–48. [PubMed: 27832421]

Madsen EL, Zagzebski JA, Banjavie RA, Jutila RE. Tissue mimicking materials for ultrasound phantoms. Med Phys 1978; 5:391–94. [PubMed: 713972]

Maeda H, Wu J, Sawa T, Matsumura Y, Hori K. Tumor vascular permeability and the EPR effect in macromolecular therapeutics: a review. J Control Release 2000; 65:271–84. [PubMed: 10699287]

Matrone G, Ramalli A, Savoia AS, Tortoli P, Magenes G. High Frame-Rate, High Resolution Ultrasound Imaging With Multi-Line Transmission and Filtered-Delay Multiply And Sum Beamforming. IEEE Trans Med Imaging 2017; 36:478–86. [PubMed: 28113492]

Rojas JD, Dayton PA. Optimizing acoustic activation of phase change contrast agents with the activation pressure matching method: A review. IEEE Trans Ultrason Ferroelectr Freq Control 2016; 64:264–72. [PubMed: 27740481]

Rojas JD, Dayton PA. In Vivo Molecular Imaging Using Low-Boiling-Point Phase-Change Contrast Agents: A Proof of Concept Study. Ultrasound Med Biol 2019a; 45:177–91. [PubMed: 30318123]

Rojas JD, Dayton PA. Vaporization Detection Imaging: A Technique for Imaging Low-Boiling-Point Phase-Change Contrast Agents with a High Depth of Penetration and Contrast-to-Tissue Ratio. Ultrasound Med Biol 2019b; 45:192–207. [PubMed: 30482709]

Seppenwoolde Y, Shirato H, Kitamura K, Shimizu S, Van Herk M, Lebesque JV, Miyasaka K. Precise and real-time measurement of 3D tumor motion in lung due to breathing and heartbeat, measured during radiotherapy. Int J Radiat Oncol Biol Phys 2002; 53:822–34. [PubMed: 12095547]

Sheeran PS, Matsunaga TO, Dayton PA. Phase change events of volatile liquid perfluorocarbon contrast agents produce unique acoustic signatures. Phys Med Biol 2013; 59:379. [PubMed: 24351961]

Sheeran PS, Rojas JD, Puett C, Hjelmquist J, Arena CB, Dayton PA. Contrast-enhanced ultrasound imaging and in vivo circulatory kinetics with low-boiling-point nanoscale phase-change perfluorocarbon agents. Ultrasound Med Biol 2015; 41:814–31. [PubMed: 25619781]

Sheeran PS, Wong VP, Luois S, McFarland RJ, Ross WD, Feingold S, Matsunaga TO, Dayton PA. Decafluorobutane as a Phase-Change Contrast Agent for Low-Energy Extravascular Ultrasonic Imaging. Ultrasound Med Biol 2011; 37:1518–30. [PubMed: 21775049]

Song PF, Zhao H, Manduca A, Urban MW, Greenleaf JF, Chen SG. Comb-Push Ultrasound Shear Elastography (CUSE): A Novel Method for Two-Dimensional Shear Elasticity Imaging of Soft Tissues. IEEE Trans Med Imaging 2012; 31:1821–32. [PubMed: 22736690]

Strohm E, Rui M, Gorelikov I, Matsuura N, Kolios M. Vaporization of perfluorocarbon droplets using optical irradiation. Biomed Opt Express 2011; 2:1432–42. [PubMed: 21698007]

Thakkar D, Gupta R, Monson K, Rapoport N. Effect of Ultrasound on the Permeability of Vascular Wall to Nano-Emulsion Droplets. Ultrasound Med Biol 2013; 39:1804–11. [PubMed: 23849384]

Tuthill TA, Baggs RB, Parker KJ. Liver-Glycogen and Water Storage - Effect on Ultrasound Attenuation. Ultrasound Med Biol 1989; 15:621–27. [PubMed: 2683289]

Whittingham TA. Contrast-specific imaging techniques: technical perspective, In: Quaia E, ed. Contrast media in ultrasonography. Berlin, Heidelberg: Springer, 2005 pp. 43–70.

Williams R, Wright C, Cherin E, Reznik N, Lee M, Gorelikov I, Foster FS, Matsuura N, Burns PN. Characterization of Submicron Phase-Change Perfluorocarbon Droplets for Extravascular Ultrasound Imaging of Cancer. Ultrasound Med Biol 2013; 39:475–89. [PubMed: 23312960]

Yang L, Cheng J, Chen Y, Yu S, Liu F, Sun Y, Chen Y, Ran H. Phase-transition nanodroplets for real-time photoacoustic/ultrasound dual-modality imaging and photothermal therapy of sentinel lymph node in breast cancer. Sci Rep 2017; 7:45213. [PubMed: 28338071]

Yoon H, Emelianov SY. Combined multiwavelength photoacoustic and plane-wave ultrasound imaging for probing dynamic phase-change contrast agents. IEEE Trans Biomed Eng 2018; 66:595–98. [PubMed: 29993455]

Yoon H, Yarmoska SK, Hannah AS, Yoon C, Hallam KA, Emelianov SY. Contrast-enhanced ultrasound imaging in vivo with laser-activated nanodroplets. Med Phys 2017; 44:3444–49. [PubMed: 28391597]

Zhang G, Harput S, Hu H, Christensen-Jeffries K, Zhu J, Brown J, Leow CH, Eckersley RJ, Dunsby C, Tang M-X. Fast Acoustic Wave Sparsely Activated Localization Microscopy (fast-AWSALM): Ultrasound Super-Resolution using Plane-Wave Activation of Nanodroplets. IEEE Trans Ultrason Ferroelectr Freq Control 2019; 66:1039–46.

Zhang G, Harput S, Lin ST, Christensen-Jeffries K, Leow CH, Brown J, Dunsby C, Eckersley RJ, Tang MX. Acoustic wave sparsely activated localization microscopy (AWSALM): Super-resolution ultrasound imaging using acoustic activation and deactivation of nanodroplets. Appl Phys Lett 2018; 113:014101.

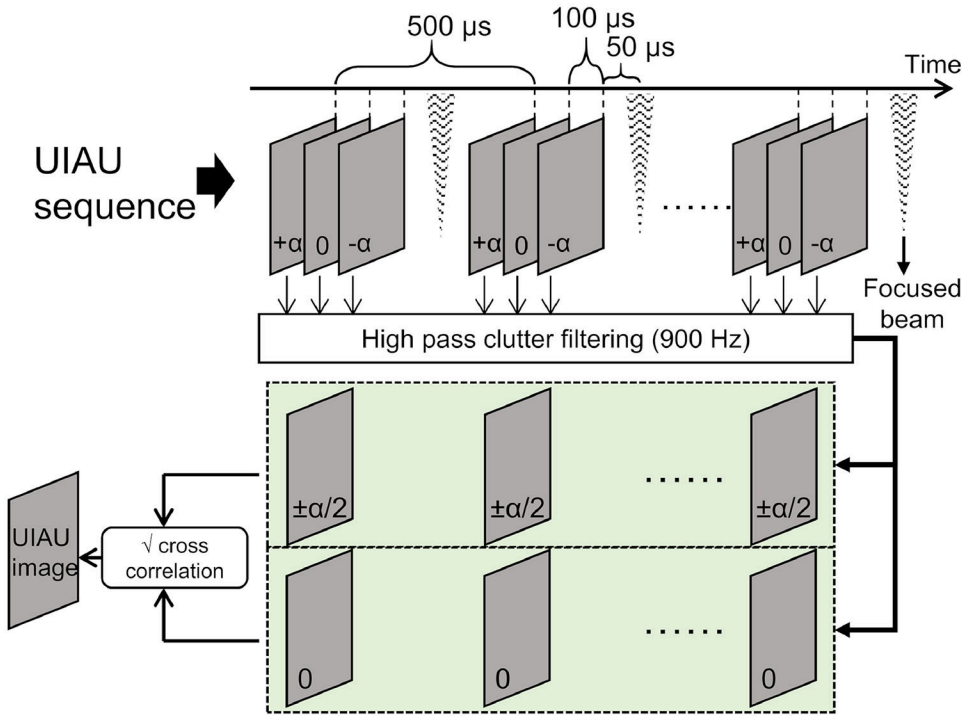

Figure 1.

Illustration of ultrafast interframe activation ultrasound (UIAU) imaging sequence and the formation of the final UIAU image of activated phase change contrast agents (PCCAs).

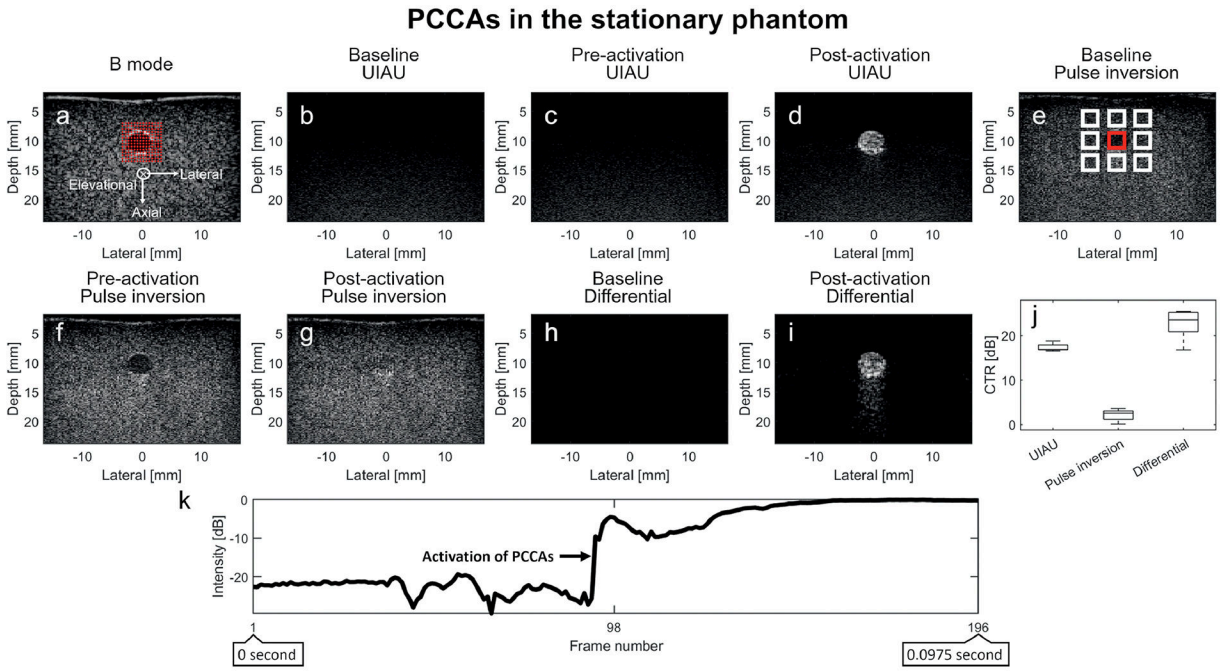

Figure 2.

Results of PCCA (phase change contrast agent) imaging in the channel of a stationary tissue-mimicking phantom. (a) B-mode ultrasound image of the phantom and channel prior to infusion of contrast agents, with red overlays indicating focal locations of PCCA activation. The axial, lateral, and elevational directions of the present coordinate system are indicated by the axes in (a); (b) Baseline UIAU image of phantom channel before PCCA infusion; (c) Pre-activation UIAU image of PCCA with the activation pulses disabled; (d) UIAU image of the PCCA in phantom channel; (e) Baseline pulse inversion image of phantom channel before PCCA infusion. (f) Pre-activation pulse inversion image of PCCAs; (g) Post-activation pulse inversion image of PCCAs; (h) Baseline differential image of the phantom before PCCA infusion; (i) Differential image of PCCAs obtained by subtracting the pre-activation B-mode IQ data from the post-activation data; (j) The contrast-to-tissue ratio (CTR) of these 3 imaging techniques in the stationary phantom. (k) The B-mode signal intensity variation of the pixel in the center of the phantom channel over the entire ensemble length (196 frames), showing persistent high intensity after PCCA activation in a single spatial location. The activation of PCCAs is indicated by the arrow in (k). The contrast (PCCA) signal magnitude is obtained by averaging the signal magnitude inside the red rectangle region in the channel, while the tissue signal magnitude is obtained from the white rectangles surrounding the phantom channel. The contrast and tissue signal magnitude are used to calculate the contrast-to-tissue ratio. The axial and lateral spacing between the regions is 1.3 mm and 2.6 mm, respectively. The baseline and pre-activation images are normalized to the post-activation PCCA images. All images are log-compressed and displayed with 30 dB dynamic range.

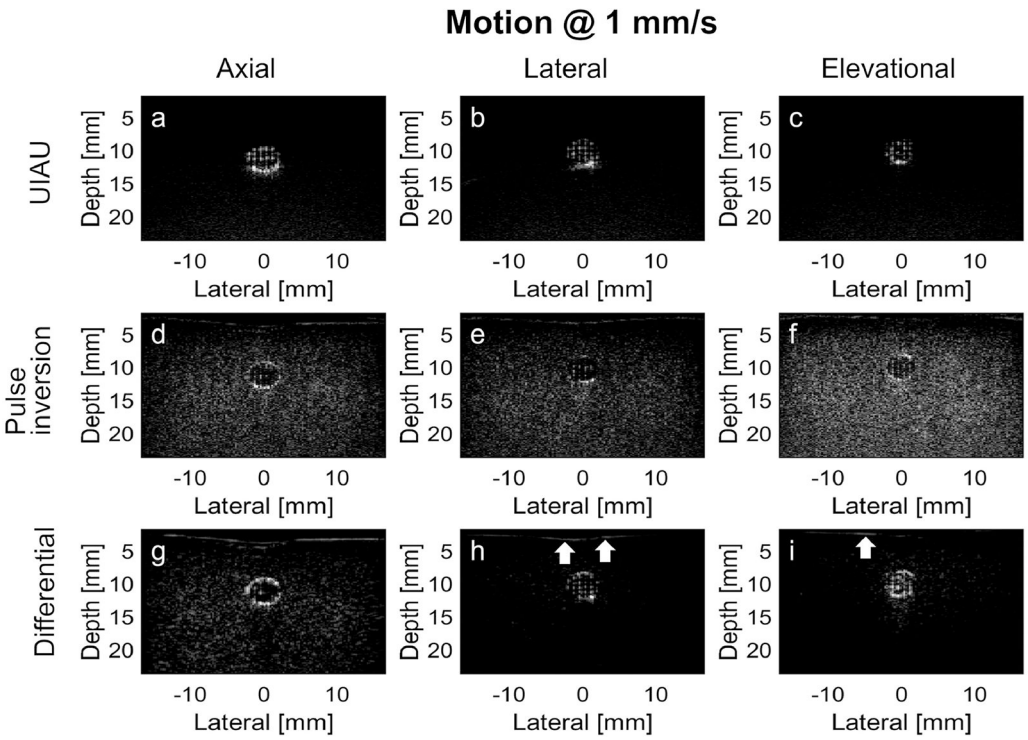

Figure 3.

Results of PCCA imaging in the channel of the tissue-mimicking phantom moving at a low motion rate (i.e., 1 mm/s). (a) UIAU image of PCCA in phantom with axial motion; (b) UIAU image of PCCA in phantom with lateral motion; (c) UIAU image of PCCA in phantom with elevational motion; (d) Pulse inversion image of PCCA in phantom with axial motion; (e) Pulse inversion image of PCCA in phantom with lateral motion; (f) Pulse inversion image of PCCA in phantom with elevational motion; (g) Differential image of PCCA in phantom with axial motion; (h) Differential image of PCCA in phantom with lateral motion; (i) Differential image of PCCA in phantom with elevational motion. The white arrows indicate the phantom-water interface in (h) and (i). All images are log-compressed and displayed with 30 dB dynamic range.

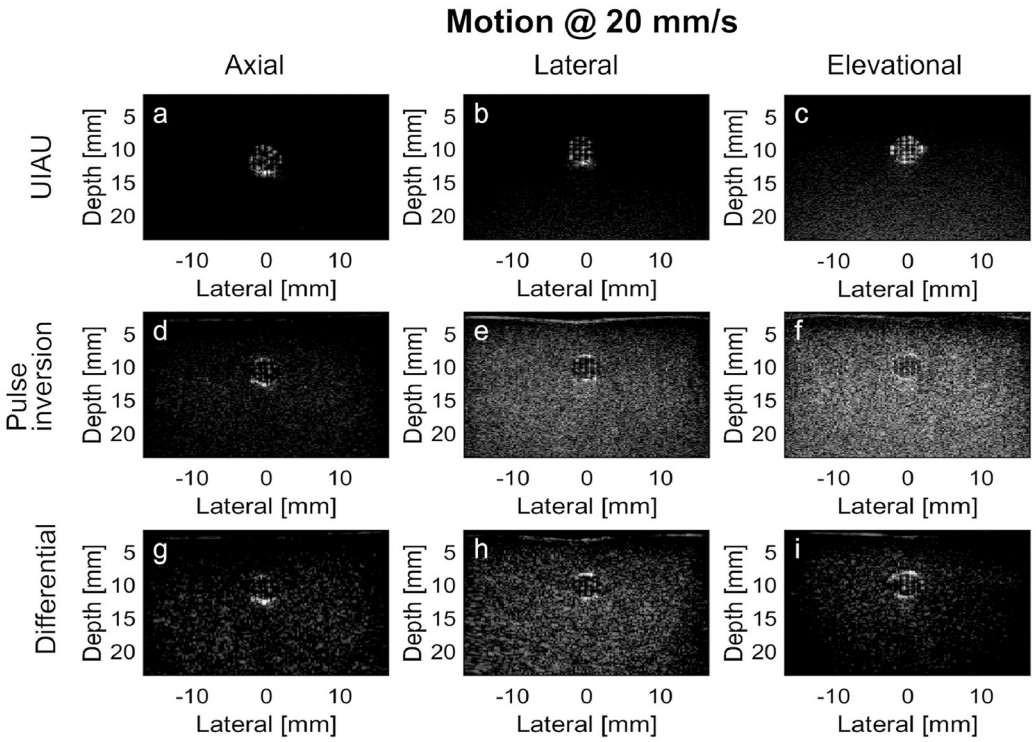

Figure 4.

Results of PCCA imaging in the channel of the tissue-mimicking phantom moving at a high motion rate (i.e., 20 mm/s). (a) UIAU image of PCCA in phantom with axial motion; (b) UIAU image of PCCA in phantom with lateral motion; (c) UIAU image of PCCA in phantom with elevational motion; (d) Pulse inversion image of PCCA in phantom with axial motion; (e) Pulse inversion image of PCCA in phantom with lateral motion; (f) Pulse inversion image of PCCA in phantom with elevational motion; (g) Differential image of PCCA in phantom with axial motion; (h) Differential image of PCCA in phantom with lateral motion; (i) Differential image of PCCA in phantom with elevational motion. All images are log-compressed and displayed with 30 dB dynamic range.

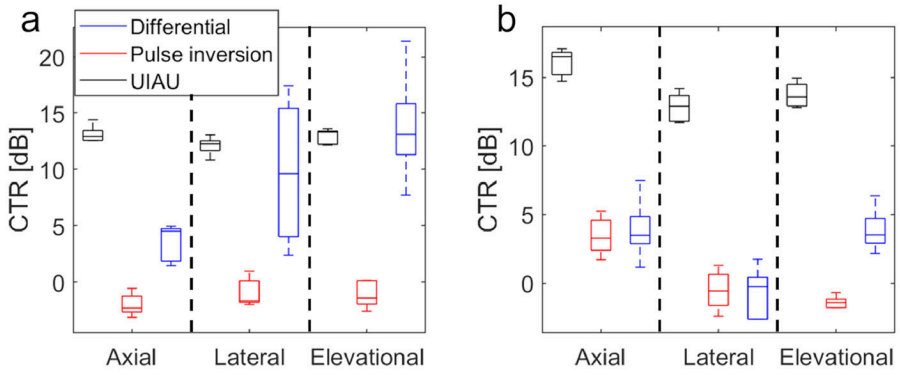

Figure 5.

The contrast to tissue ratio (CTR) of 3 imaging techniques (i.e., UIAU, pulse inversion and differential imaging); (a) The CTR at a low motion rate (i.e., 1 mm/s). (b) The CTR at a high motion rate (i.e., 20 mm/s).

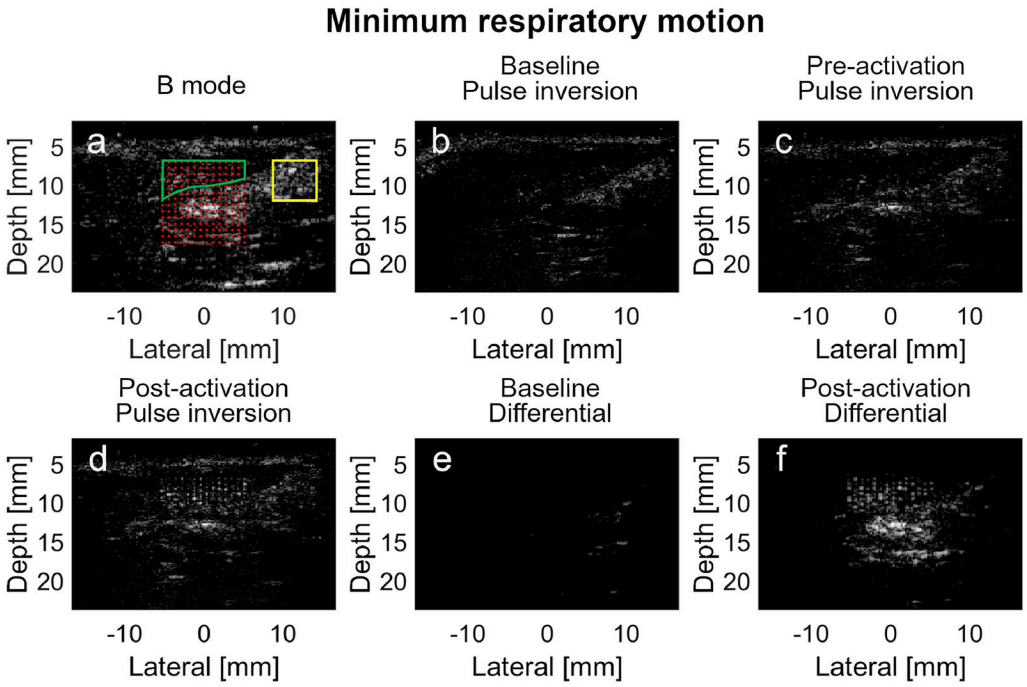

Figure 6.

In vivo imaging of the PCCA in rat liver during minimum respiratory motion using pulse inversion and differential imaging techniques. (a) Pre-activation B-mode image with superimposed activation beam focal locations. The overlap region between the liver and the activation foci, where the baseline, pre-activation and post-activation PCCAs signal magnitudes are calculated, is indicated by the green boundary. The region outside the PCCA activation zone, where the signal magnitude of the echogenic clutter is calculated, is indicated by the yellow rectangle boundary. (b) Baseline pulse inversion image of the liver before the PCCAs are injected; (c) Pre-activation pulse inversion image after the PCCAs are injected; (d) Post-activation pulse inversion image of the PCCAs; (e) Baseline differential image of the phantom before the PCCAs are injected; (f) Differential image of the PCCAs after injection. Baseline and pre-activation images are all normalized to the post-activation images. All images are log-compressed and displayed with 30 dB dynamic range.

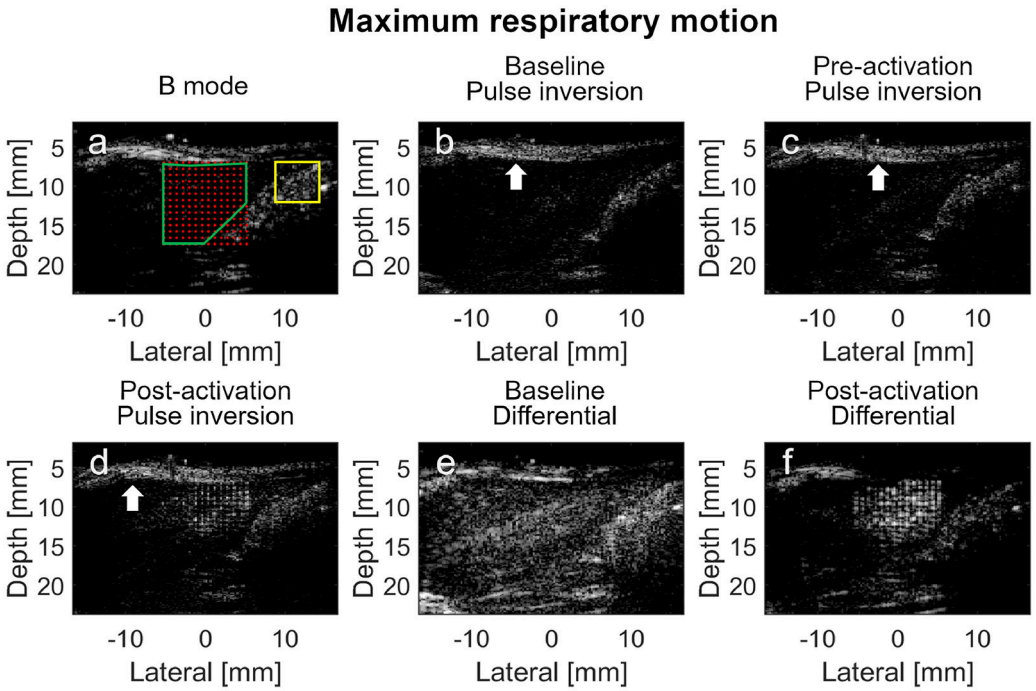

Figure 7.

In vivo imaging of the PCCA in rat liver during maximum respiratory motion using pulse inversion and differential imaging techniques. (a) Pre-activation B-mode image with superimposed activation beam focal locations. The overlap region between the liver and the activation foci, where the baseline, pre-activation and post-activation PCCAs signal magnitudes are calculated, is indicated by the green boundary. The region outside the PCCA activation zone, where the signal magnitude of the echogenic clutter is calculated, is indicated by the yellow rectangle boundary. (b) Baseline pulse inversion image of the liver before the PCCAs are injected; (c) Pre-activation pulse inversion image after the PCCAs are injected; (d) Post-activation pulse inversion image of the PCCAs; (e) Baseline differential image of the phantom before the PCCAs are injected; (f) Differential image of the PCCAs after injection. The white arrows indicate the skin layer. Baseline and pre-activation images are all normalized to the post-activation images. All images are log-compressed and displayed with 30 dB dynamic range.

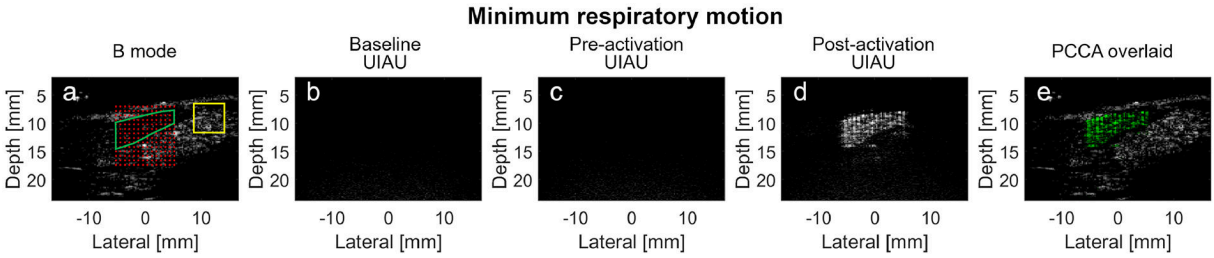

Figure 8.

In vivo imaging of the PCCA in rat liver during minimum respiratory motion using the UIAU imaging technique. (a) Pre-activation B-mode image with superimposed activation beam focal locations. The overlap region between the liver and the activation foci, where the baseline, pre-activation and post-activation PCCAs signal magnitudes are calculated, is indicated by the green boundary. The region outside the PCCA activation zone, where the signal magnitude of the echogenic clutter is calculated, is indicated by the yellow rectangle boundary. (b) Baseline UIAU image of the liver before the PCCAs are injected; (c) Pre-activation UIAU image of the PCCA with the activation pulses turned off; (d) UIAU image of the vaporized PCCA; (e) PCCA image in (d), shown in green, overlaid on the B-mode image (a) (grayscale); Baseline and pre-activation images are all normalized to the post-activation images. All images are log-compressed and displayed with 30 dB dynamic range.

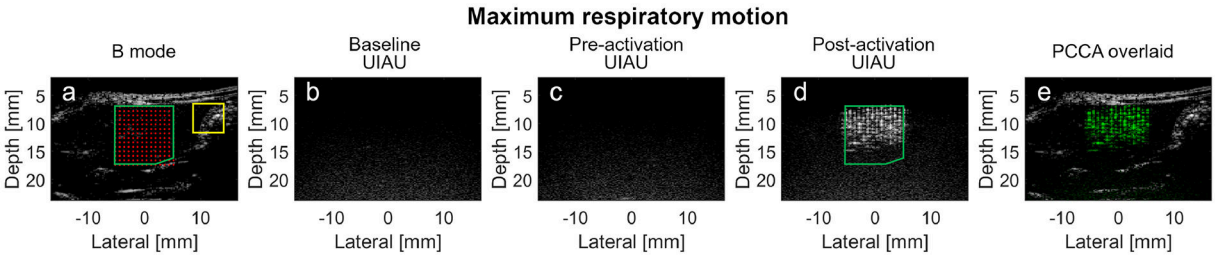

Figure 9.

In vivo imaging of the PCCA in rat liver during maximum respiratory motion using the UIAU imaging technique. (a) Pre-activation B-mode image with superimposed activation beam focal locations. The overlap region between the liver and the activation foci, where the baseline, pre-activation and post-activation PCCAs signal magnitudes are calculated, is indicated by the green boundary. The region outside the PCCA activation zone, where the signal magnitude of the echogenic clutter is calculated, is indicated by the yellow rectangle boundary. (b) Baseline UIAU image of the liver before the PCCAs are injected; (c) Pre-activation UIAU image of the PCCA with the activation pulses turned off; (d) UIAU image of the vaporized PCCA; (e) PCCA image in (d), shown in green, overlaid on the B-mode image (a) (grayscale); Baseline and pre-activation images are all normalized to the post-activation images. All images are log-compressed and displayed with 30 dB dynamic range.

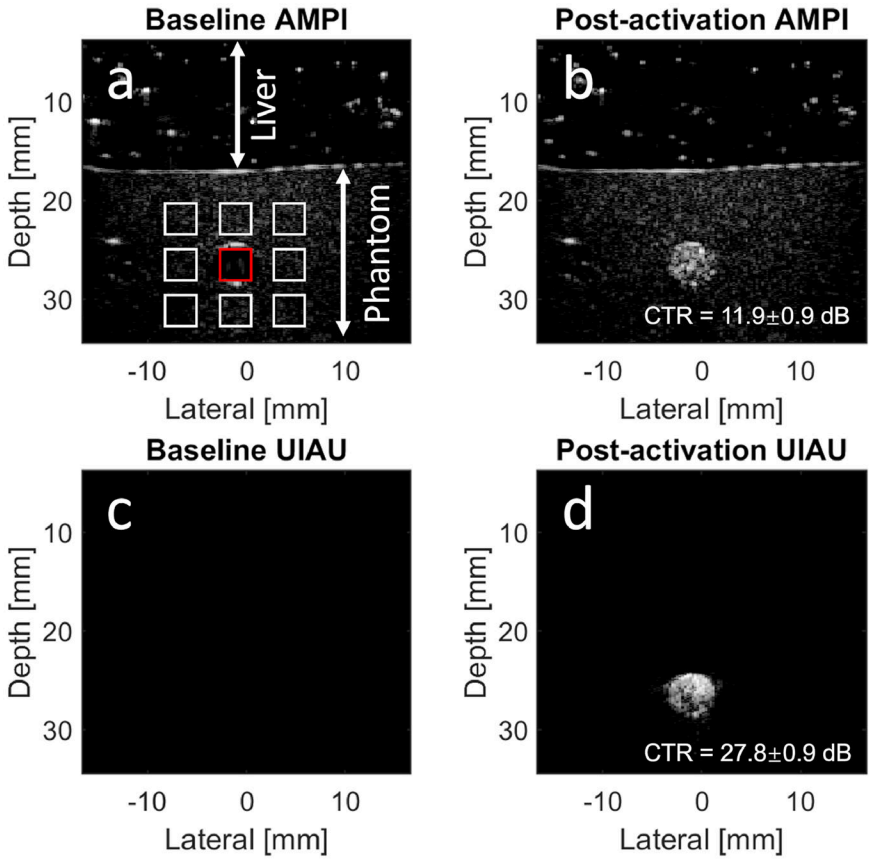

Figure 10.

Imaging PCCAs at a depth of 25 mm. (a) Baseline amplitude modulation pulse inversion (AMPI) image without PCCAs in the phantom channel. A porcine liver sample was placed on the top of the phantom. The contrast (PCCA) signal magnitude is obtained by averaging the signal magnitude inside the red rectangle region in the channel, while the tissue signal magnitude is obtained from the white rectangles surrounding the phantom channel. The contrast and tissue signal magnitude are used to calculate the contrast-to-tissue ratio (CTR). (b) Post-activation AMPI image with the CTR; (c) Baseline ultrafast interframe activation ultrasound (UIAU) image; (d) Post-activation UIAU image with the CTR. All images are log-compressed and displayed with 30 dB dynamic range.